Extracting the morphology of gold bipyramids from SAXS experiments via form factor modeling

Jieli Lyu, Claire Goldmann, Cyrille Hamon, Doru Constantin

▶ **To cite this version:**

Jieli Lyu, Claire Goldmann, Cyrille Hamon, Doru Constantin. Extracting the morphology of gold bipyramids from SAXS experiments via form factor modeling. Journal of Applied Crystallography, 2023, 56 (1), pp.214-221. ⟨10.1107/S1600576722011669⟩. ⟨hal-03956176⟩

HAL Id: hal-03956176

https://hal.science/hal-03956176v1

Submitted on 25 Jan 2023

HAL is a multi-disciplinary open access archive for the deposit and dissemination of scientific research documents, whether they are published or not. The documents may come from teaching and research institutions in France or abroad, or from public or private research centers.

L'archive ouverte pluridisciplinaire **HAL**, est destinée au dépôt et à la diffusion de documents scientifiques de niveau recherche, publiés ou non, émanant des établissements d'enseignement et de recherche français ou étrangers, des laboratoires publics ou privés.

HAL Authorization

Extracting the morphology of gold bipyramids from SAXS experiments via form factor modeling

Jieli Lyu, Claire Goldmann, and Cyrille Hamon*

Laboratoire de Physique des Solides, CNRS, Univ. Paris-Sud, Université Paris-Saclay, 91405 Orsay Cedex, France

Doru Constantin†

Institut Charles Sadron, CNRS and Université de Strasbourg, 67034 Strasbourg, France

(Dated: January 25, 2023)

Abstract

Accurate shape description is a challenge in material science. Small-angle X-ray scattering (SAXS) can provide the shape, size and polydispersity of nanoparticles by form factor modeling. However, simple geometrical models such as the ellipsoid may not be enough to describe objects with complex shapes. In this work we show that the form factor of gold nanobipyramids is accurately described by a truncated bicone model, which is validated by comparison with transmission electron microscopy (TEM) data for nine different synthesis batches: we obtain the average shape parameters (width, height, and truncation) and the sample polydispersity. In contrast, the ellipsoid model yields worse fits of the SAXS data and exhibits systematic discrepancies with the TEM results.

Keywords: SAXS,colloids,bipyramids,form factor,TEM

* cyrille.hamon@universite-paris-saclay.fr

† constantin@unistra.fr

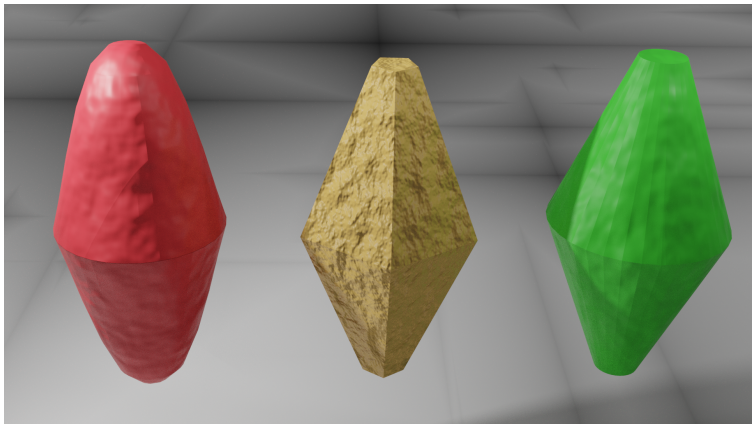

I. INTRODUCTION

Recent progress in materials chemistry has allowed the synthesis of nanoparticles with very well defined shape and size [1]. In order to stay relevant, characterization techniques must also evolve to keep up with this progress. Form factors for a wide variety of shapes have therefore been implemented in many small-angle scattering software suites [2–6], but their analytical expressions can be quite complicated and the numerical evaluation very time-consuming, especially since a double integral over the orientation is usually required.

An alternative (model-free) strategy consists in describing the objects as a collection of small beads (also referred to as dummy atom models, or DAMs) [7]. The number and positions of these "atoms" are then adjusted until the scattering signal of the model approaches the experimental data. Initially developed for the study of biological macromolecules, this approach has recently been applied to inorganic nanocrystals [8–10]. We do not consider these models here, for two main reasons: the difficulty of converting between DAMs and geometrical shapes (which are very good descriptions for the nanoparticles we are interested in) and that of accounting for polydispersity, although some progress has been made on the latter aspect [11].

A natural question to ask in this context is: how detailed must the models be in order to extract as much information as possible about the morphology of the objects? Is it really useful to go beyond simple shapes, such as spheres or ellipsoids? The answer is a resounding "yes" in the case of cubes. Previous work [12] has shown that the difference between cubes and rhombocuboctahedra in composite Au@Ag objects is both detectable by SAXS and important in view of applications. In our group, we have followed by SAXS the morphological transition from spheres to cubes in such objects and confirmed these results

by TEM [13]. A noteworthy conclusion is that both the asphericity and the polydispersity reduce the amplitude of the characteristic oscillations of the sphere form factor, but in slightly different ways: the former reduces the contrast of the fringes and preserves their number and overall profile, while the latter "smears" them in the manner of a Debye-Waller factor. Although both are isometric, cubes and spheres are easily distinguished if monodisperse enough. Moreover, these shapes are instances of a more general family, that of the superball. The position of the nanoparticles along the continuum defined by the associated shape parameter can be estimated via SAXS [14] and modulates the particle packing in supercrystals [15].

Introducing anisometry (by elongating or flattening the object of interest) renders the problem more complicated, unless the resulting object has a constant section (as in a rod or a plate). Since they are amenable to factorization, these limiting cases are easily treated analytically and have been extensively used in the literature. Let us note that factorization can also be used in the case of curved plates, considerably simplifying the calculations [16].

Here, we are specifically interested in spindles, elongated objects whose section varies along the length (so factorization does not apply): are they adequately described by their equivalent ellipsoids (with an appropriate polydispersity), or would we benefit from using more realistic models? The experimental system we have investigated consists of gold nanobipyramids (Au NBPs). The synthesis of these objects was refined over the last decade and the interest in their optical properties and subsequent applications has grown constantly [17–19]. Advanced modeling and simulations have shown how the optical response of the objects (e.g. the position of the surface plasmon resonance) depends on shape features such as the truncation [20–22]. The precise morphology of the NBPs influences their assembly in two [23, 24] or three [25] dimensions, which in turn further modulates their optical properties.

Accurate characterization of the Au NBPs is therefore imperative in view of any applications. The shape information can of course be obtained by TEM, but SAXS and other scattering techniques exhibit two major advantages: they are non-intrusive (and thus can investigate synthesis, reshaping or assembly processes) and they average over a large collection of objects (obviating the statistical issues that might affect imaging techniques). On the downside, they only yield indirect and orientation-averaged information: the comparison with TEM is of course needed for validating the models.

In this paper, we describe Au NBPs as truncated bicones: the model is used to extract

morphological parameters (from both SAXS and TEM data) and compared to the simpler ellipsoid model. Extensive analysis of the results obtained with nine different synthesis batches shows that the bicone model is accurate enough to capture the width, height opening angle (or, equivalently, truncation) and polydispersity of the particles, while the ellipsoid model exhibits systematic discrepancies or, in the case of the opening angle, simply does not account for this feature.

II. METHODS

A. Materials

Gold chloride trihydrate ($HAuCl_4 \cdot 3\,H_2O \geq 99.9\%$), silver nitrate ($AgNO_3 > 99\%$), hydrochloric acid (HCl 37%), sodium borohydride ($NaBH_4 \geq 96\%$), L-ascorbic acid (AA, $\geq 99\%$), trisodium citrate dihydrate ($\geq 99\%$), cetyltrimethylammonium bromide (CTAB $\geq 99\%$), cetyltrimethylammonium chloride (CTAC, 25 wt % in H_2O), and benzyldimethylhexadecylammonium chloride (BDAC 99%) were purchased from Merck. Water purified by reverse osmosis with a resistivity above 15 MΩ.cm) was used in all experiments.

B. Bipyramid Synthesis and Purification

Au NBPs were synthesized as described previously [21, 26, 27].

a. Seed synthesis 2.65 mL of CTAC (25wt % in water) and 33 mL of water were heated at 30 °C. Then, 400 μL of $HAuCl_4 \cdot 3\,H_2O$ (25 mM) and 4 mL of trisodium citrate (50 mM) were added and the mixture was kept at 30 °C for 30 minutes. Under fast stirring, 1 mL of $NaBH_4$ (25 mM) was added quickly. Stirring was continued for 1 minute and the resulting solution was put in the oven for 5 days at 40 °C prior to use.

b. Growth of particle batches A to D 2 mL of $AgNO_3$ (10 mM), 4 mL of $HAuCl_4 \cdot 3\,H_2O$ (25 mM), and 4 mL of HCl (1 M) were added in 200 mL of CTAB (100 mM). Then, 1.6 mL of AA (100 mM) was added, followed by a various amount of seeds: 3.5, 3.5, 3.6, 3.6 mL for samples A to D. After 4 h at 30 °C, the bipyramids were centrifuged twice and purified by depletion during one night at 30 °C in 15 mL BDAC (350 mM) [28]. The supernatant was removed, and the precipitate was redispersed in water and washed twice with 1 mM CTAC. The Au NBPs were finally redispersed in 2 mL of 1 mM CTAC.

c. Growth of particle batches E to I The protocol was in all points similar to that used for samples A to D, except the solution volumes were halved and the final CTAC concentration was 2.5 mM. The seed volumes were: 5, 2, 1, 1 and 0.1 ml for samples E to I.

C. TEM

The solutions were concentrated by slow centrifugation to a final Au^0 concentration of 0.75 mM in 0.55 mM CTAC. 10 μL of this solution was then dropped on a carbon-coated grid and dried at 70 °C. Transmission electron microscopy (TEM) images were obtained with a JEOL 1400 microscope, operating at an acceleration voltage of 120 kV.

The bicone model is defined as in Figure 1: The total width is denoted by W, the total (effective) length by L, and the total length of the bicone (without truncation) is H. The truncation $t = (H - L)/2$ and the full tip angle is α. These parameters are not independent, so in the following we will use the set (W, L, α) to fully describe the shape of one particle. The ellipsoid model only has two parameters, the major and minor axes a and b, which correspond to W and L of the bicone model, as the length along the symmetry axis and the transverse diameter, respectively. For a complete description of the particle population in one sample we also need the polydispersity p (to be discussed below).

The TEM images are treated using Igor Pro 7.0 [29]: first, the particles are separated from the background using a bimodal fit: ImageThreshold operation, with the M=(2) option. The contours of each particle are then identified using the ImageAnalyzeParticles operation, with options /E/W/M=3/FILL/EBPC. Option /E computes the equivalent ellipse for each particle, defined by the five parameters (X_c, Y_c, a, b, θ): x and y coordinates of the particle center, major and minor semi-axes and orientation angle. They are used as a first approximation for the bicone shape (or, more precisely, for its plane projection: a truncated diamond, see Figure 1).

Both the extracted contour and the model are represented in polar coordinates (as $R_e(\phi)$ and $R_m(\phi)$, respectively) and the difference between them quantified as $\chi^2 = \int \mathrm{d}\phi |R_e(\phi) - R_m(\phi)|^2$. Optimizing χ^2 is not straightforward, but we obtained good results by a two-step approach: simulated annealing (which is more robust, but does not always reach the minimum) followed by line search (to further refine the parameter values). Both steps are performed using the Optimize operation, with options $M = \{3, 0\}$ and $M = \{0, 0\}$ (default),

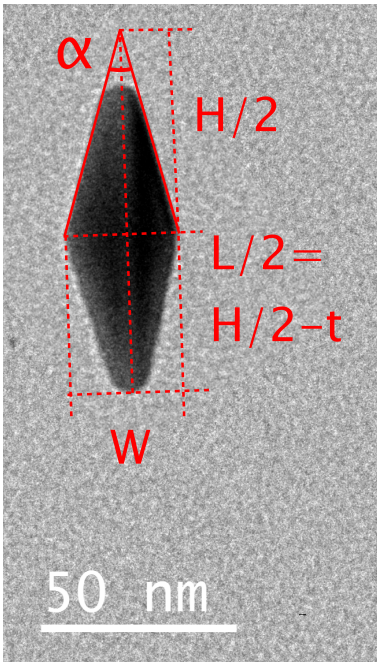

FIG. 1. TEM image of a particle, with the morphology parameters of the bicone model.

respectively.

The extracted contour and the model are then presented to the user for inspection. We reject inadequately fitted contours, composite objects (where several particles are superposed and cannot be discriminated), and some round objects (possibly spheres or unreacted decahedral seeds).

D. SAXS

SAXS measurements were performed on the SWING beamline of the SOLEIL synchrotron (Saint-Aubin, France) at a beam energy of $E = 16\,\mathrm{keV}$. The sample-to-detector distance was 6.22 m, covering a scattering vector range $0.0014 < q < 0.24\text{Å}^{-1}$. The beam size was approximately $500 \times 200\mu\mathrm{m}^2$ (H × V). All measurements were performed at room temperature (22 °C). The scattered signal was recorded by an Eiger 4M detector (Dectris Ltd., Switzerland) with pixel size 75μm. Preliminary data treatment (angular averaging and normalization) was done using the software Foxtrot developed at the beamline [**?**], which yielded the intensity as a function of the scattering vector $I(q)$ in absolute units. Models for the ellipsoid and the bicone were implemented in Igor Pro 7.0: more details are available in the Appendix. Polydispersity is accounted for by a homothetic Gaussian size distribution

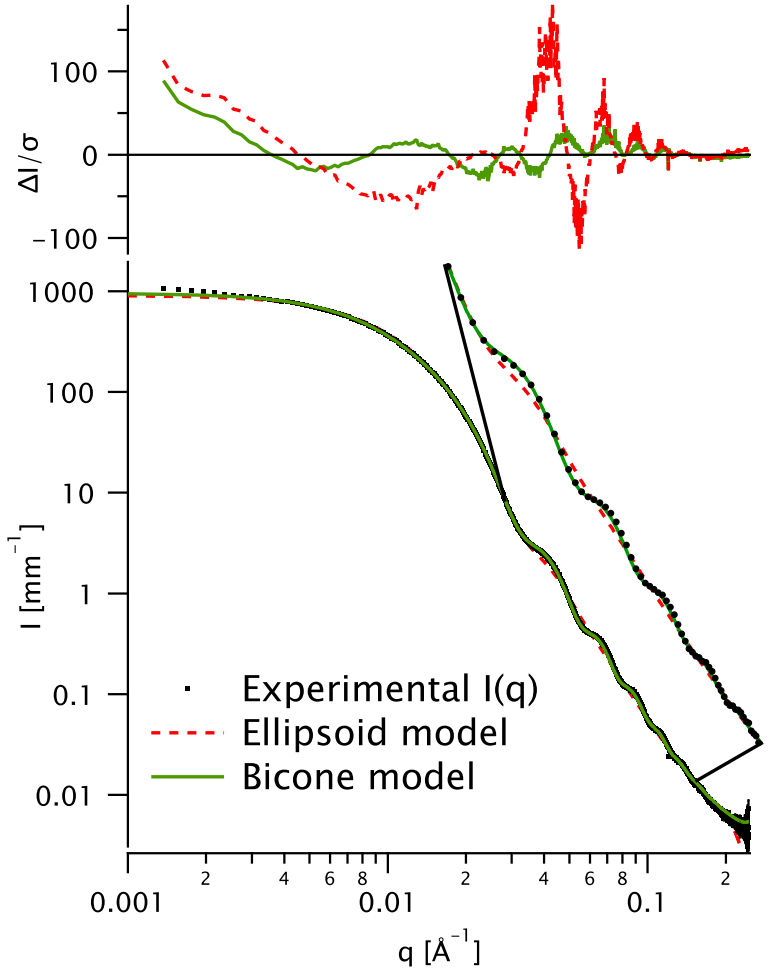

FIG. 2. Fits to the scattering data for sample A (black dots) with the ellipsoid (red dashed line) and bicone (solid green line) models. The residues are shown in the top panel. A zoomed-in view of the oscillations is shown to the right: for clarity, only one data point in ten is displayed.

(affecting all dimensions similarly) with relative standard deviation p.

III. RESULTS AND DISCUSSION

A. SAXS

A detailed fit example is shown in Figure 2 for sample A. Fits for the other samples (B-I) are shown in Figure 3.

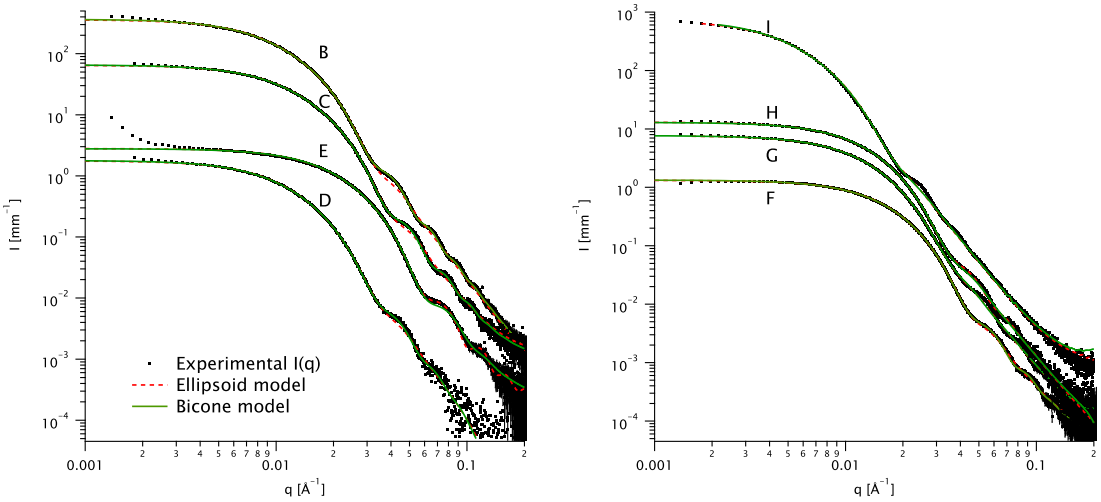

FIG. 3. Fits to the scattering data for samples B through I (black dots) with the ellipsoid (red dashed line) and bicone (solid green line) models.

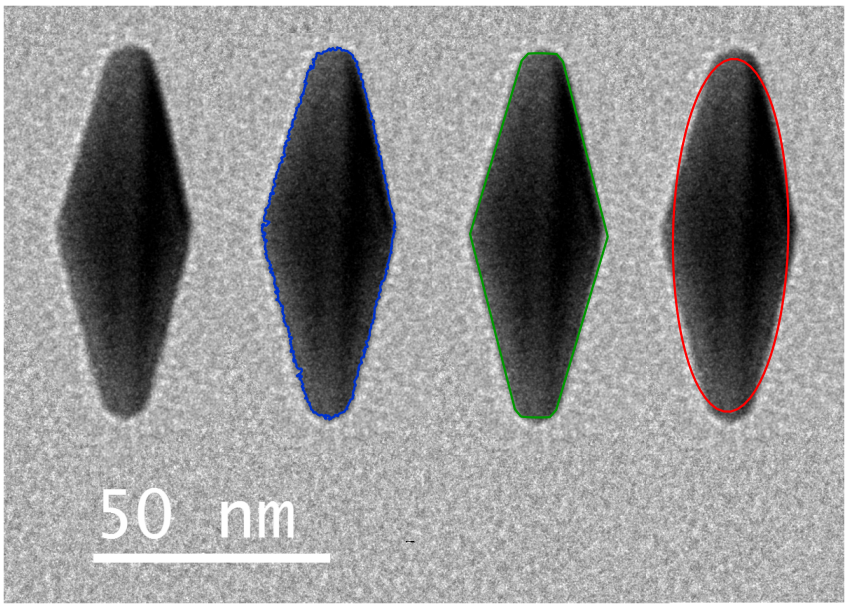

FIG. 4. Four copies of the TEM image of one particle (from solution H). From left to right: naked image, with detected contour (blue), with bipyramid fit (green) and with ellipse fit (red).

B. TEM

A fit example is shown in Figure 4 for one particle from sample H.

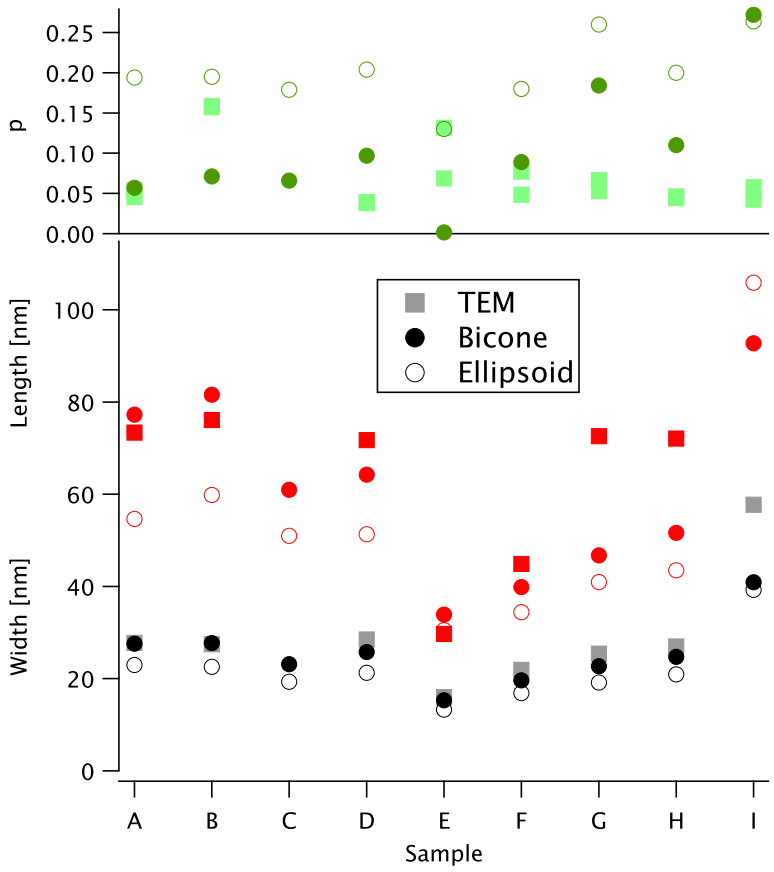

FIG. 5. Fit parameters for the bicone and ellipsoid models compared with the TEM values. Top panel: polydispersity p (green symbols). Middle panel: total length (red). Bottom panel: total width (black and gray). The symbols are the same for all panels: solid dots for the bicone model, open dots for the ellipsoid model, squares for the TEM data.

C. Comparison

Three fit parameters, the total length and width, represented by (L, W) for the bicone model and by (a, b) for the ellipsoid model as well as the polydispersity p can be directly compared between the two models. They are presented in Figure 5 for all nine samples; the TEM data is also shown for comparison, except for sample C, where this data is not available. Note that the TEM analysis yields two values of p, as the ratio of the standard deviation to the mean value for L and W, respectively. By definition, the SAXS models only include one p value.

The (full) tip angle α is only accounted for by the bicone model (and, of course, by the

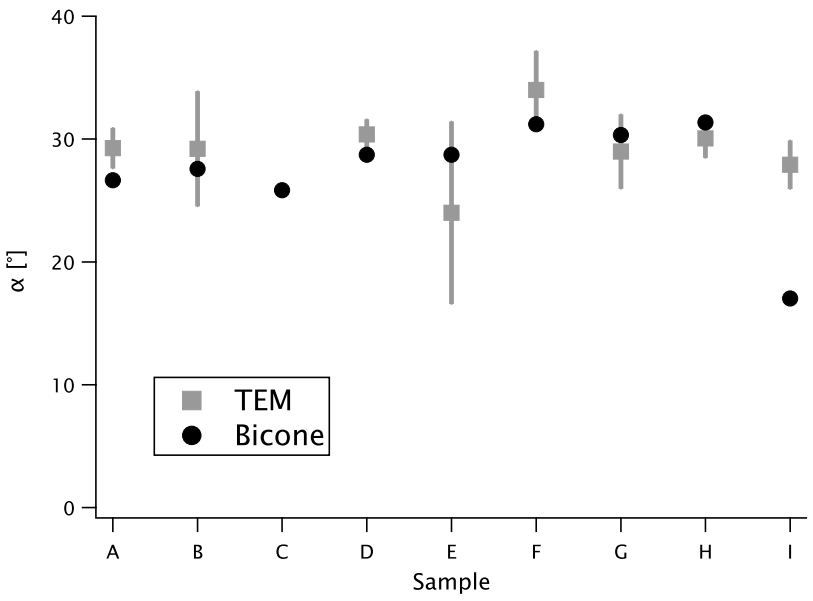

FIG. 6. Tip angle α obtained from the bicone model (solid dots for the best fit values; error bars are smaller than the symbol size) compared with the TEM values (squares and error bars; mean $\pm$ SD).

TEM analysis). This parameter is shown in Figure 6. Except for sample C (where the TEM data is lacking) and for sample I (where the fit quality is low), the BC values are always within the standard deviation of the TEM distribution.

Note that the ellipsoid model *cannot* measure α (or, conversely, the virtual length H). One could of course build an angle β from the aspect ratio, e.g. as $\tan(\beta) = W/L$, but this is an arbitrary choice and would severely overestimate the true tip angle, because it neglects truncation: β is between 41° and 52° for all our samples.

All fit parameters and some other details are given in Table I. The AS curves are presented in Appendix B and representative TEM images are shown in Appendix C. Both the bicone and the ellipsoid models yield bad fits for sample I: in particular, the polydispersity is severely overestimated (see Figure 3 and Table I), because the particle shape is often irregular (see Figure 9). This is because the attempted particle size (about 150 nm long) is at the upper limit for NBP synthesis: above it, one obtains nanojavelins [21].

TABLE I. Parameters obtained by the three techniques (AS, SAXS and TEM) for all samples.

Technique	SAXS							TEM								AS		
Parameter	L	W	a	b	α	p_{BC}	p_{Ell}	L	W	a	b	α	p_{L}	p_{W}	N_{part}[a]	λ_{max}[b]	$\Delta\lambda$[c]	Peak ratio[d]
Unit	[nm]	[nm]	[nm]	[nm]	°	–	–	[nm]	[nm]	[nm]	[nm]	°	–	–	–	[nm]	[nm]	–
A	77.3	27.6	54.6	22.9	26.6	0.057	0.194	73.4	27.7	72.6	23.9	29.3	0.0541	0.0454	156	743	55	7.15
B	81.6	27.7	59.8	22.6	27.6	0.071	0.195	76.1	27.5	73.5	23	29.2	0.159	0.157	47	751	57	6.75
C	61	23.1	51	19.3	25.8	0.066	0.179									759	56	7.85
D	64.2	25.8	51.3	21.3	28.7	0.097	0.204	71.7	28.5	71.2	24.3	30.4	0.0379	0.0393	31	743	56	5.23
E	33.9	15.3	30.5	13.3	28.7	0.0014	0.13	29.7	16	31.7	14.5	24	0.131	0.0685	143	668	58	3.21
F	39.9	19.6	34.4	16.9	31.2	0.089	0.18	44.9	21.9	45.7	19.1	34	0.0771	0.0482	25	731	57	4.62
G	46.7	22.7	41	19.2	30.3	0.184	0.26	72.6	25.4	70.6	21.3	29	0.0527	0.0667	39	808	60	5.55
H	51.6	24.7	43.5	20.9	31.4	0.11	0.2	72.1	27	70.5	22.9	30.1	0.0462	0.0442	67	774	58	3.6
I	92.7	40.9	106	39.3	17	0.272	0.264	153	57.7	153	49.3	27.9	0.0578	0.0424	12	957	113	5.39

[a] Number of particles used in the analysis.

[b] Position of the longitudinal plasmon peak.

[c] Width of the longitudinal plasmon peak.

[d] Between the intensity of the longitudinal and the transverse plasmon peaks.

IV. CONCLUSION

The ellipsoid model yields reasonable values for the length and width of the objects, although they are always slightly underestimated. The polydispersity is significantly overestimated, and the tip angle cannot be inferred from this model.

On the other hand, the bicone model clearly yields much better fits to the SAXS data than the ellipsoid one and the resulting coefficients are in very good agreement with the TEM results, in particular for the tip angle α. We conclude that this model is appropriate for describing Au NBPs. Potential applications include monitoring the growth of these objects in solution, but also the evolution of composite nanoparticles obtained by the deposition of a different metal (e.g. silver) onto Au NBPs [30, 31].

The SAXS data and the two models presented in this work are available as supporting information.

Appendix A: Form factor models and fit quality

1. Ellipsoid

The ellipsoid form factor is implemented as in the NIST SANS macros [2]: due to the symmetry of the NBPs, we only consider spheroids (with major axes $a \neq b = c$). All fits yield prolate results (with $a > b$).

2. Bicone

The form factor for a (full or truncated) cone is given in the literature, e.g. in [32], and implemented in SASFIT [3] and BornAgain [6]. For completeness, we present here its derivation for a truncated bicone, using the notation in Figure 1. Since the body has azimuthal symmetry (around the z axis), we can assume without loss of generality that the scattering vector $\mathbf{q}$ is contained in the (x, z) plane: $\mathbf{q} = (q_r, 0, q_z)$, and makes an angle θ with the z axis. The transverse radius of the complete cone at any height z between $-H$ and H is given by:

$$r(z) = R\left(1 - \frac{|z|}{H}\right)$$

.

The form factor of the object is:

$$F(\mathbf{q}) = \int_{\mathbb{R}^3} \mathrm{d}r^3 \mathrm{e}^{-i\mathbf{qr}} \rho(\mathbf{r}) = \Delta\rho \int_{\mathcal{V}} \mathrm{d}r^3 \mathrm{e}^{-i\mathbf{qr}}$$

where $\rho(\mathbf{r})$ is the scattering length density (SLD), which depends on the space position. $\Delta\rho$ is the SLD difference between the object (which is homogeneous and occupies the volume $\mathcal{V}$) and the surrounding medium. In cylindrical coordinates, the current vector is: $\mathbf{r} = (\xi, \phi, z)$, where the azimuthal angle ϕ is measured with respect to the x axis and the phase factor $\mathrm{e}^{-i\mathbf{qr}} = \mathrm{e}^{-i\xi q_r \cos(\phi)} \mathrm{e}^{-iq_z z}$. We can express the form factor as:

$$\begin{aligned} F(\mathbf{q}) &= \Delta\rho \int_{-(H/2-t)}^{H/2-t} \mathrm{d}z\, \mathrm{e}^{-iq_z z} \int_0^{r(z)} \xi \mathrm{d}\xi \int_0^{2\pi} \mathrm{d}\phi\, \mathrm{e}^{-i\xi q_r \cos(\phi)} \\ &= 2\pi\Delta\rho \int_{-(H/2-t)}^{H/2-t} \mathrm{d}z\, \mathrm{e}^{-iq_z z} \int_0^{r(z)} \xi \mathrm{d}\xi J_0(\xi q_r) \\ &= 2\pi\Delta\rho \int_{-(H/2-t)}^{H/2-t} \mathrm{d}z\, r^2(z)\, \mathrm{e}^{-iq_z z} \frac{J_1[q_r r(z)]}{q_r r(z)} \\ &= 4\pi\Delta\rho \int_0^{H/2-t} \mathrm{d}z\, r^2(z)\, \cos(q_z z) \frac{J_1[q_r r(z)]}{q_r r(z)}. \end{aligned} \tag{A1}$$

For a fixed amplitude $q = |\mathbf{q}|$ of the scattering vector, the formula above yields the form factor for a given orientation θ. In solution, the scattering signal results from an incoherent average over all orientations, so the relevant quantity is:

$$\begin{aligned} P(q) &= \left\langle |F(\mathbf{q})|^2 \right\rangle_\theta \\ &= \int_0^\pi \sin(\theta) \mathrm{d}\theta |F((q\cos(\theta), 0, q\sin(\theta)))|^2. \end{aligned} \tag{A2}$$

3. Polydispersity

In both the ellipsoid and the bicone models we account for the polydispersity by introducing a homothetical size distribution: all dimensions are scaled by a parameter λ with respect to their reference ($\lambda = 1$) values (W_0, L_0, α) or (a_0, b_0) –in which case the scattered signal is $I_0(q)$– and λ is distributed along a Gaussian:

$$g(\lambda) = \frac{1}{\sqrt{2\pi}\, p} \exp\left[-\frac{1}{2} \left(\frac{\lambda - 1}{p} \right)^2 \right] \tag{A3}$$

Scaling all sizes by λ or the scattering vector q by the same factor preserves the signal, up to a λ^6 prefactor (easily understood if we recall that the scattered intensity is proportional

TABLE II. Goodness-of-fit χ^2 obtained with the bicone and ellipsoid models for all samples (data and fits in Figures 2 and 3.).

Sample	χ^2_{BC}	χ^2_{Ell}
A	103.2	1112
B	14.8	51.5
C	7.4	20.5
D	2.9	4.0
E	18.0	22.7
F	3.6	8.0
G	19.8	18.6
H	4.9	8.5
I	115.8	134.2

to the particle volume squared.) The polydisperse signal can then be obtained as:

$$I_{\mathrm{avg}}(q) = \int \mathrm{d}\lambda\, g(\lambda) I_\lambda(q) = \int \mathrm{d}\lambda\, g(\lambda) \lambda^6 I_0(\lambda q) \tag{A4}$$

Relation (A4) applies to any particle shape. In particular, we checked that the sphere model yields very close results to the analytical Schulz distribution as implemented in Igor Pro [2].

This algorithm has the advantage of being very fast, as it requires only one calculation of the form factor (for the reference values of the dimensions), followed by the averaging step (A4). It is also very general, applying to homogeneous or composite nanoparticles of any shape. Its only disadvantage is the intrinsic limitation to homothetical polydispersity.

4. Fit quality

There is a significant difference in fit quality between the two models, but it is difficult to discern from the graphs in Figures 2 and 3. We give the goodness-of-fit χ^2 for both models in Table II:

Appendix B: UV-Vis-IR absorbance spectroscopy

Absorbance spectroscopy (AS) is the most common technique for characterizing plasmonic nanoparticles. In Figure 7, we present the spectra of all samples, normalized to an extinction value of 0.5 at 400 nm.

Appendix C: TEM images

We present in Figures 8 and 9 representative images for all samples.

Appendix D: Distance distribution function

In Figure 10 we present the distance distribution function $P(r)$ for some samples, computed using the denss.fit_data routine in the DENSS suite [33]. For ease of comparison, the curves are normalized to 1 at the mode. We could not obtain reliable $P(r)$ values for curves E, F and I, presumably due to small-q imperfections (for the first two) and to the large particle size for the last one.

ACKNOWLEDGMENTS

JL acknowledges financial support by the China Scholarship Council (CSC). The authors acknowledge SOLEIL for the provision of synchrotron radiation facilities (experiment 20201118) and Thomas Bizien for help using the SWING beamline. The present work has benefited from the electronic microscopy facility of Imagerie-Gif, (http://www.i2bc.paris-saclay.fr), member of IBiSA (http://www.ibisa.net), supported by "France-BioImaging" (ANR10-INBS-04-01), and the Labex "Saclay Plant Science" (ANR-11-IDEX-0003-02).

---

[1] X. Lu, M. Rycenga, S. E. Skrabalak, B. Wiley, and Y. Xia, Annual review of physical chemistry **60**, 167 (2009).

[2] S. R. Kline, Journal of Applied Crystallography **39**, 895 (2006).

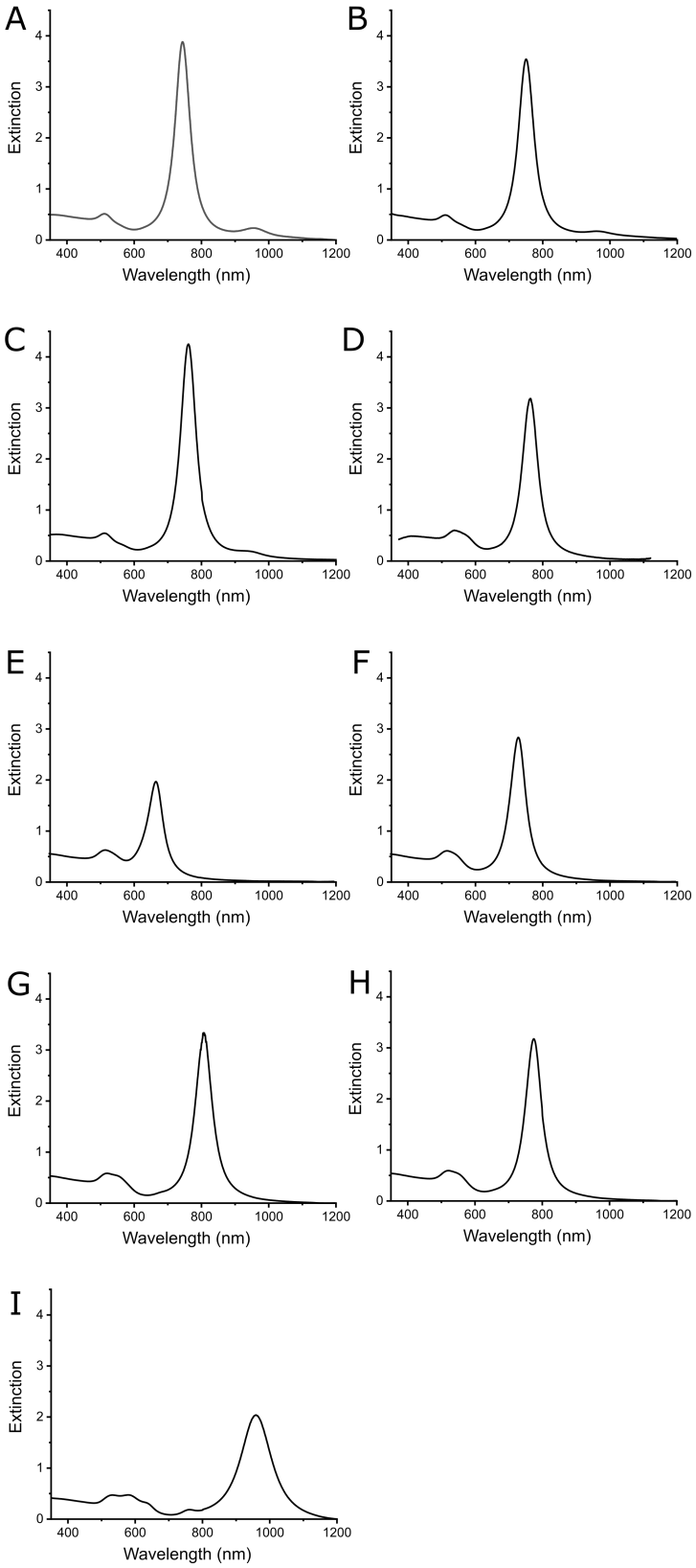

FIG. 7. AS spectra for all samples.

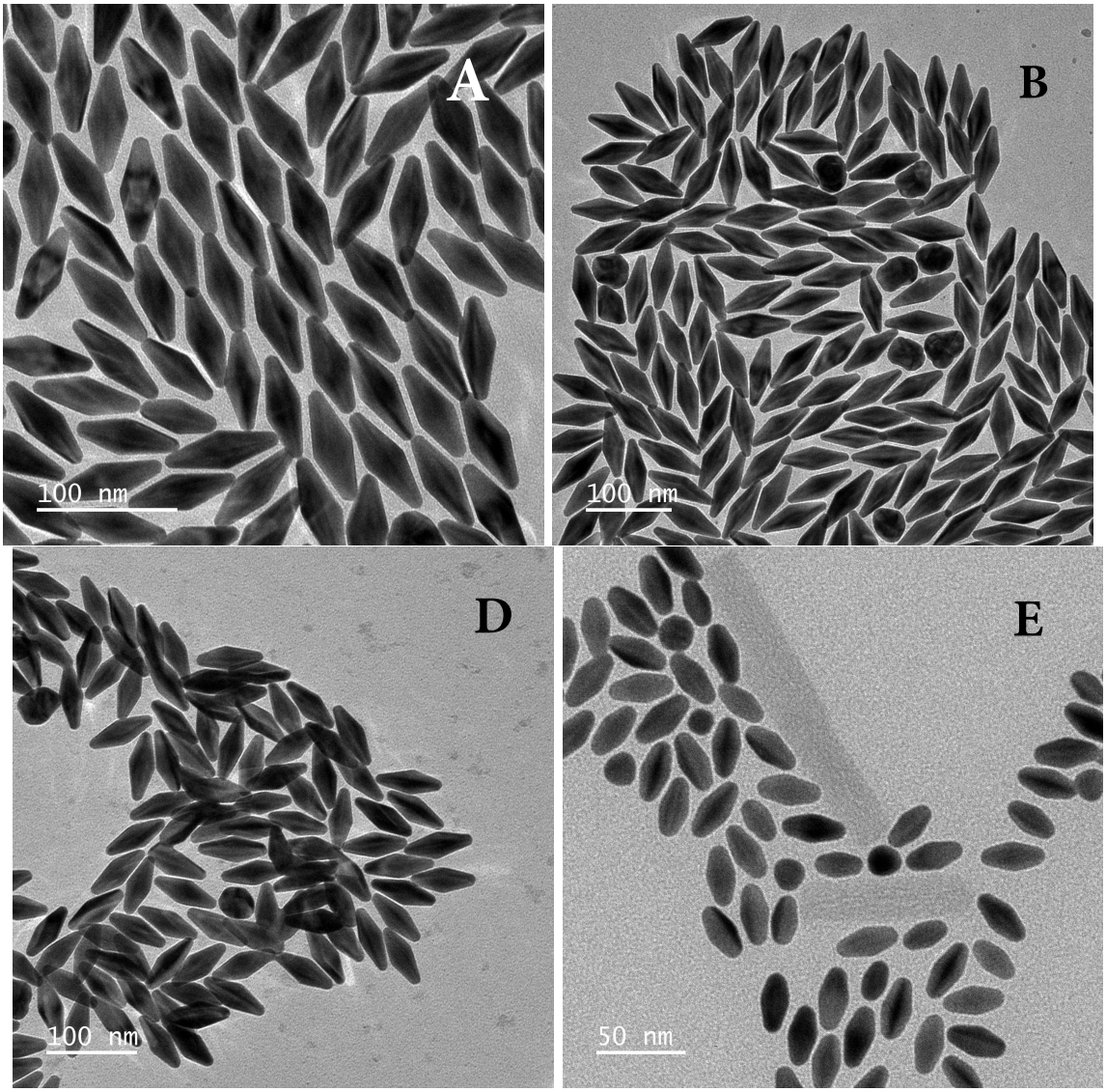

FIG. 8. TEM images for samples A, B, D and E.

[3] I. Breßler, J. Kohlbrecher, and A. F. Thünemann, Journal of Applied Crystallography **48**, 1587 (2015).

[4] M. Doucet, J. H. Cho, G. Alina, S. King, P. Butler, P. Kienzle, J. Krzywon, A. Jackson, T. Richter, M. Gonzales, T. Nielsen, R. Ferraz Leal, A. Markvardsen, R. Heenan, P. Juhas, J. Bakker, P. Rozyczko, W. Potrzebowski, L. O'driscoll, K. Campbell, and A. Washington, "SasView version 4.0," Zenodo (2016).

[5] A. Ginsburg, T. Ben-Nun, R. Asor, A. Shemesh, L. Fink, R. Tekoah, Y. Levartovsky, D. Khaykelson, R. Dharan, A. Fellig, and U. Raviv, Journal of Applied Crystallography **52**, 219 (2019).

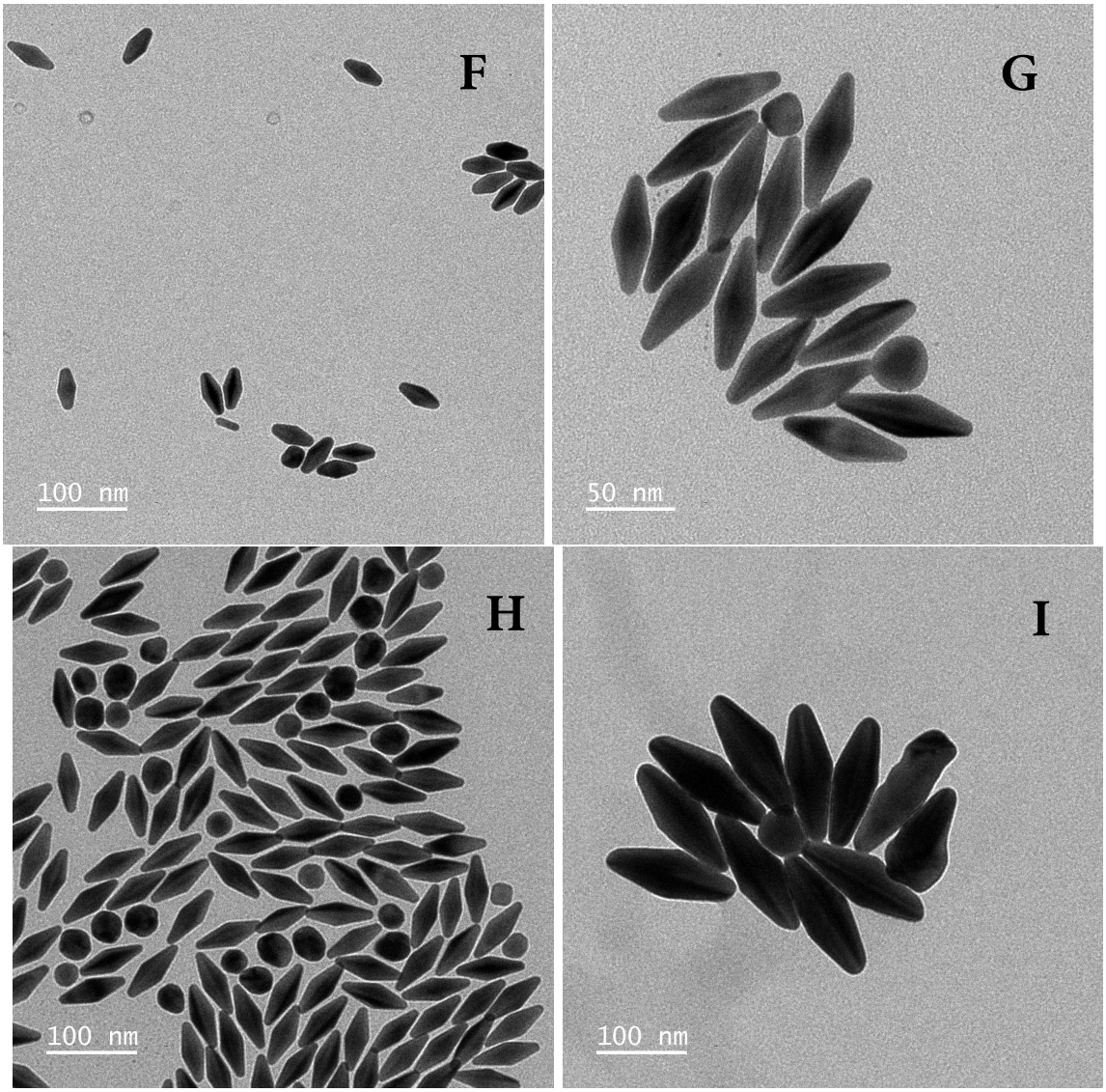

FIG. 9. TEM images for samples F to I. The image of sample H was taken prior to purification, which explains the large number of spheres still present. Most of them are no longer present in the final sample.

[6] G. Pospelov, W. Van Herck, J. Burle, J. M. Carmona Loaiza, C. Durniak, J. M. Fisher, M. Ganeva, D. Yurov, and J. Wuttke, Journal of Applied Crystallography **53**, 262 (2020).

[7] D. I. Svergun, Biophysical Journal **76**, 2879 (1999).

[8] M. Burian, G. Fritz-Popovski, M. He, M. V. Kovalenko, O. Paris, and R. T. Lechner, Journal of Applied Crystallography **48**, 857 (2015).

[9] M. Burian, C. Karner, M. Yarema, W. Heiss, H. Amenitsch, C. Dellago, and R. T. Lechner, Advanced Materials **30**, 1802078 (2018).

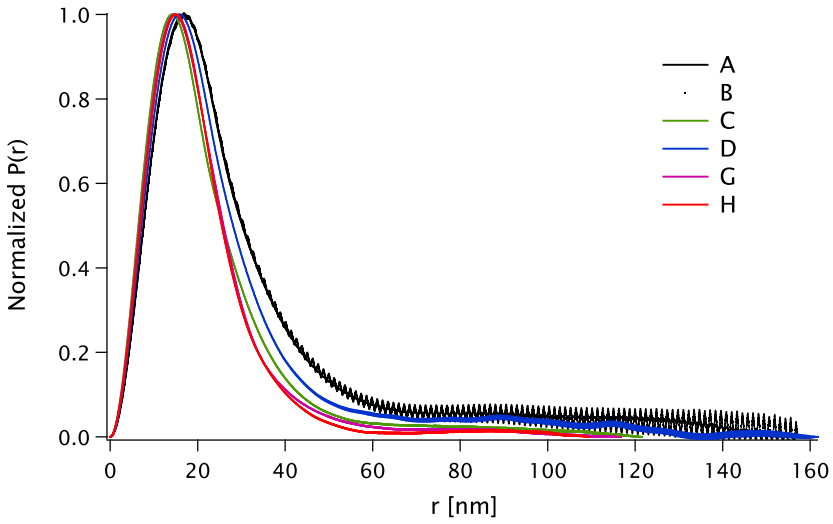

FIG. 10. Distance distribution function $P(r)$ for samples A, B, C, D, G and H.

[10] M. Burian and H. Amenitsch, IUCrJ **5**, 390 (2018).

[11] P. V. Konarev, V. V. Volkov, and D. I. Svergun, Journal of Physics: Conference Series **747**, 012036 (2016).

[12] A. M. Steiner, M. Mayer, D. Schletz, D. Wolf, P. Formanek, R. Hübner, M. Dulle, S. Förster, T. A. Koenig, and A. Fery, Chemistry of Materials **31**, 2822 (2019).

[13] J. Lyu, V. Geertsen, C. Hamon, and D. Constantin, Nanoscale Advances **2**, 4522 (2020).

[14] D. Dresen, A. Qdemat, S. Ulusoy, F. Mees, D. Zákutná, E. Wetterskog, E. Kentzinger, G. Salazar-Alvarez, and S. Disch, The Journal of Physical Chemistry C **125**, 23356 (2021).

[15] J.-M. Meijer, A. Pal, S. Ouhajji, H. N. W. Lekkerkerker, A. P. Philipse, and A. V. Petukhov, Nature Communications **8**, 14352 (2017).

[16] D. Constantin, Journal of Applied Crystallography **48**, 1901 (2015).

[17] R. Arenal, L. Henrard, L. Roiban, O. Ersen, J. Burgin, and M. Treguer-Delapierre, The Journal of Physical Chemistry C **118**, 25643 (2014).

[18] W. Rao, Q. Li, Y. Wang, T. Li, and L. Wu, ACS Nano **9**, 2783 (2015).

[19] Z. Mai, Y. Yuan, J.-S. B. Tai, B. Senyuk, B. Liu, H. Li, Y. Wang, G. Zhou, and I. I. Smalyukh, Advanced Science **8**, 2102854 (2021).

[20] M. Liu, P. Guyot-Sionnest, T.-W. Lee, and S. K. Gray, Physical Review B **76**, 235428 (2007).

[21] D. Chateau, A. Liotta, F. Vadcard, J. R. G. Navarro, F. Chaput, J. Lermé, F. Lerouge, and S. Parola, Nanoscale **7**, 1934 (2015).

[22] J. Marcheselli, D. Chateau, F. Lerouge, P. Baldeck, C. Andraud, S. Parola, S. Baroni, S. Corni, M. Garavelli, and I. Rivalta, Journal of Chemical Theory and Computation **16**, 3807 (2020).

[23] Q. Shi, K. J. Si, D. Sikdar, L. W. Yap, M. Premaratne, and W. Cheng, ACS Nano **10**, 967 (2016).

[24] R. Fu, D. E. Gómez, Q. Shi, L. W. Yap, Q. Lyu, K. Wang, Z. Yong, and W. Cheng, Nano Letters **21**, 389 (2021).

[25] J. Lyu, W. Chaâbani, E. Modin, A. Chuvilin, T. Bizien, F. Smallenburg, M. Impéror-Clerc, D. Constantin, and C. Hamon, Advanced Materials **34**, 2200883 (2022).

[26] A. Sánchez-Iglesias, N. Winckelmans, T. Altantzis, S. Bals, M. Grzelczak, and L. M. Liz-Marzán, Journal of the American Chemical Society **139**, 107 (2017).

[27] X. Li, J. Lyu, C. Goldmann, M. Kociak, D. Constantin, and C. Hamon, The Journal of Physical Chemistry Letters **10**, 7093 (2019).

[28] J.-H. Lee, K. J. Gibson, G. Chen, and Y. Weizmann, Nature Communications **6**, 7571 (2015).

[29] `https://www.wavemetrics.com/products/igorpro`.

[30] C. Goldmann, M. De Frutos, E. H. Hill, D. Constantin, and C. Hamon, Chemistry of Materials **33**, 2948 (2021).

[31] C. Goldmann, X. Li, M. Kociak, D. Constantin, and C. Hamon, The Journal of Physical Chemistry C **126**, 11667 (2022).

[32] G. Renaud, R. Lazzari, and F. Leroy, Surface Science Reports **64**, 255 (2009).

[33] T. D. Grant, Nature Methods **15**, 191 (2018).